Fluidization of elongated particles—Effect of multi-particle correlations for drag, lift, and torque in CFD-DEM

Mema, Ivan; Padding, Johan T.

Important note
To cite this publication, please use the final published version (if applicable).
Please check the document version above.

Fluidization of elongated particles—Effect of multi-particle correlations for drag, lift, and torque in CFD-DEM

Ivan Mema [ORCID] | Johan T. Padding

Complex Fluid Processing, Department of Process and Energy, Delft University of Technology, Delft, The Netherlands

Correspondence
Ivan Mema, Complex Fluid Processing, Department of Process and Energy, Delft University of Technology, Leeghwaterstraat 39, Delft 2628 CB, The Netherlands.
Email: i.mema@tudelft.nl

Abstract

Having proper correlations for hydrodynamic forces is essential for successful CFD-DEM simulations of a fluidized bed. For spherical particles in a fluidized bed, efficient correlations for predicting the drag force, including the crowding effect caused by surrounding particles, are already available and well tested. However, for elongated particles, next to the drag force, the lift force, and hydrodynamic torque also gain importance. In this work, we apply recently developed multi-particle correlations for drag, lift and torque in CFD-DEM simulations of a fluidized bed with spherocylindrical particles of aspect ratio 4 and compare them to simulations with widely used single-particle correlations for elongated particles. Simulation results are compared with previous magnetic particle tracking experimental results. We show that multi-particle correlations improve the prediction of particle orientation and vertical velocity. We also show the importance of including hydrodynamic torque.

KEYWORDS
CFD-DEM, fluidized bed, hydrodynamic torque, lift force, multi-particle correlations, nonspherical particles

1 | INTRODUCTION

Fluidized beds are irreplaceable equipment in industry as they offer the highest contact between solid particles and gas, together with rapid mixing of particles and most efficient heat transfer between gas and solids. Due to their industrial importance, fluidized beds have been subject of numerous experimental and numerical research over the past century. Thanks to the advancements in computer performance in recent decades, many numerical models, able to successfully simulate operation of industrial scale fluidized beds with spherical particles have been developed. Usage of such models considerably reduce the time and costs of optimization and development of the processes that rely on fluidized beds. Coupled CFD-DEM is viewed as one of the most accurate models in fluidized bed research because it fully resolves particle–particle interactions while particle-fluid interactions are resolved through closures for hydrodynamic forces. Having closures that can accurately predict the hydrodynamic forces experienced by the particles in a fluidized bed is crucial for successful usage of CFD-DEM models.

A considerable number of processes in industry rely on usage of fluidized beds for manipulating granular materials where the particle shape is nonspherical. This is specifically the case for processes where biomass is used. The biomass is usually dried, milled, and processed into pellets. These kinds of particles are considerably larger than powder like materials usually used in fluidized beds and are characterized by an elongated shape. Existing numerical models, developed for fluidization of spherical particles, cannot be applied to fluidization of these kinds of particles as elongated particles will have much more complex particle–particle interactions together with orientation dependent hydrodynamic forces. Our previous investigation[1] showed that

additional forces like shape induced lift force and hydrodynamic torque have considerable effect on fluidization of elongated particles and cannot be neglected.

While fluidization of spherical particles is thoroughly investigated and there is a number of accurate and well tested drag correlations for spherical particles available in literature,[2] this is not the case for elongated particles. When it comes to the drag force experienced by a single elongated particle, a few correlations are available in literature. Haider and Levenspiel[3] presented a drag correlation based on particle sphericity, which however did not take into account particle orientation. Ganser[4] on the other hand proposed a drag correlation based on Stokes' and Newton's shape factors. More recently, Hölzer and Sommerfeld[5] introduced a general drag force correlation based on particle sphericity, crosswise and lengthwise sphericity, and Reynolds number, while Zastawny et al.[6] and Sanjeevi et al.[7] proposed correlations for specific particle shapes. Quite recently, Cao et al.[8] developed the drag correlation for suspensions of ellipsoidal particles that takes into account solids fraction, Reynolds number and particle inclination and geometry. So far, the correlation by Hölzer and Sommerfeld[5] has been widely applied in fluidization of nonspherical particles, as it proved to be the most flexible. For shape induced lift force and hydrodynamic torque on elongated particles, the only correlations available in literature are proposed by Zastawny et al.,[6] Ouchene et al.,[9] and Sanjeevi et al.[7]

During fluidization, particles rarely find themselves isolated in a fluidized bed, but are most of the time surrounded by other particles in dense fluidizing conditions. The surrounding particles in dense fluidizing conditions can have an effect on hydrodynamic forces experienced by a particle. For spherical particles there are correlations that takes into account this effect of the surrounding particles. The first one that bridged dilute and dense particulate conditions was the expression by Di Felice.[10] Recently, Tenneti et al.[11] and Tang et al.[12] proposed new expressions for static assemblies of spheres, and Rong et al.[13] suggested extension of the Di Felice equation. For nonspherical particles the multi-particle (MP) effect only recently came into the spotlight when Li et al.[14] discussed the drag and lift force and He and Tafti[15] the drag, lift and torque on assemblies of ellipsoidal particles. So far, the only correlations for drag, lift, and torque applicable to elongated particles that take into account the effect of surrounding particles, have been proposed by Sanjeevi et al.[16] However, this correlations has not been applied in CFD-DEM simulations so far, and their influence on fluidization is still unknown.

In this work, we investigate the effect of MP correlations for hydrodynamic forces and torque on the fluidization characteristics of elongated, spherocylindrical particles with aspect ratio 4 using CFD-DEM simulations. Simulations with Sanjeevi MP correlations[16] are compared to simulations with the Hölzer and Sommerfeld drag model,[5] expanded with Di Felice expression[10] and lift and torque correlations proposed by Zastawny et al.[6] for an isolated particle. For validation, the simulation results are compared with experimental results previously obtained using magnetic-particle tracking (MPT).[17]

2 | NUMERICAL MODEL

The CFD-DEM algorithm used in this work is based on open source software, namely OpenFoam to solve the fluid equations (CFD) and LIGGGHTS to solve the particle equations (DEM). These two algorithms are coupled using open source CFDEM coupling.[18] The open source codes were adapted so that they can be applied to spherocylindrical particles without relying on a MP approach. More in-depth information about the model and its validation can be found in previous work.[1,19]

2.1 | Discrete element model

The interaction between particles is modeled using the discrete element model (DEM), a soft contact model first introduced by Cundall and Strack[20] to describe interaction between granular particles. In model used in this work soft sphere contact model is adapted to deal with spherocylindical particles, where particle position, geometry, and orientation are defined and tracked. The translational motion for particle i can be calculated by integrating the expression

$$m_i \frac{d\mathbf{v}_i}{dt} = \sum_j \left(\mathbf{F}_{ij,n} + \mathbf{F}_{ij,t} \right) + \mathbf{F}_{i,f} + \mathbf{F}_{i,p} + \mathbf{F}_{i,b} \tag{1}$$

where the sum runs over all neighbors j in contact with particle i, $\mathbf{F}_{ij,n}$ is the normal contact force acting on particle i due to its interaction with particle j, $\mathbf{F}_{ij,t}$ is the tangential contact force acting on particle i due to its interaction with particle j, $\mathbf{F}_{i,f}$ is the total hydrodynamic force acting on the particle, $\mathbf{F}_{i,p}$ represents the pressure gradient (buoyancy) force acting on the particle and $\mathbf{F}_{i,b}$ is anybody force acting on the particle including gravity. The rotational motion of a particle i can be solved using

$$\frac{d(\mathbf{I}_i \cdot \boldsymbol{\omega}_i)}{dt} = \sum_j \mathbf{T}_{ij} + \mathbf{T}_{i,f} \tag{2}$$

where $\mathbf{I}_i$ is the particle moment of inertia tensor, $\boldsymbol{\omega}_i$ is the angular velocity of the particle, $\mathbf{T}_{ij}$ is the contact torque acting on the particle i due to its interaction with neighboring particle j, and $\mathbf{T}_{i,f}$ is the fluid-induced pitching torque. Unlike for spherical particles where the contact torque $\mathbf{T}_{ij}$ is only caused by tangential contact forces, in the case of nonspherical particles the torque is caused by *both* tangential and normal contact forces.

Inter-particle forces develop only when particles spatially overlap. Two adjacent spherocylindrical particles are overlapping when the distance between their shafts $|\mathbf{S}_2 - \mathbf{S}_2|$ to be smaller then sum of their radii (2R) as shown in Figure 1. An algorithm for calculating the shortest distance between shafts is presented by Vega and Lago,[21] and more detailed information about its application in the used model can be found in.[1,19]

To calculate the normal contact force exerted on particle P_1 by particle P_2 we use a linear spring-dashpot model such that the normal contact force is given by
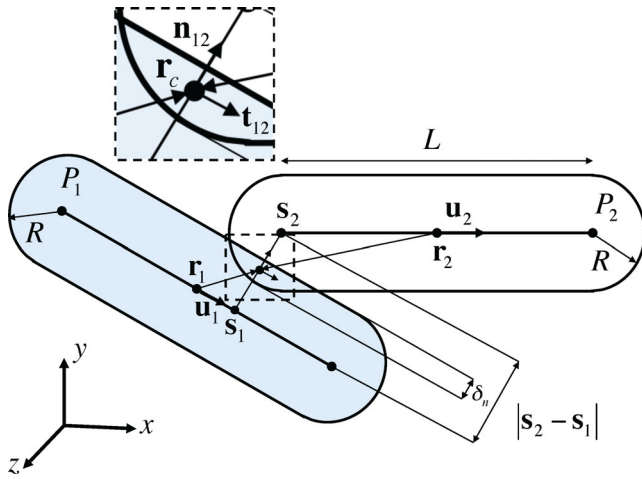
FIGURE 1 A schematic of a sample contact between two spherocylinders with each having a shaft length l, a total length L, and a characteristic radius R. The inset image shows of the normal and tangential unit vectors at the contact [Color figure can be viewed at wileyonlinelibrary.com]

$$\mathbf{F}_{12,n} = -k_n\delta_n\mathbf{n}_{12} - \eta_n\mathbf{v}_{12,n} \tag{3}$$

where k_n is the normal spring constant, η_n is the normal damping coefficient and $\mathbf{v}_{12,n}$ is the normal relative velocity between the particles. As shown in Equation (3), the normal contact force is dependent on the degree of overlapping distance δ_n, which is calculated with the aforementioned collision detection scheme for spherocylinders.

The magnitude of the tangential contact force is calculated from the Coulomb-type friction expression

$$\mathbf{F}_{12,t} = \begin{cases} -k_t\delta_t - \eta_t\mathbf{v}_{12,t} & \text{if}\,|\mathbf{F}_{12,t}| \leq \mu|\mathbf{F}_{12,n}| \\ -\mu|\mathbf{F}_{12,n}|\mathbf{t}_{12} & \text{if}\,|\mathbf{F}_{12,t}| > \mu|\mathbf{F}_{12,n}| \end{cases} \tag{4}$$

In this expression $\mathbf{t}_{12}$ is tangential unit vector defined as $\mathbf{t}_{12} = \mathbf{v}_{12}/|\mathbf{v}_{12}|$, k_t, δ_t, η_t, μ, and $\mathbf{v}_{12,t}$ are the tangential spring constant, tangential overlap, tangential damping coefficient, friction coefficient, and tangential relative velocity, respectively. δ_t is calculated from the time integral of the tangential relative velocity since the development of the initial particle contact and given by

$$\delta_t = \int_{t_{c,0}}^{t} \mathbf{v}_{12,t} dt \tag{5}$$

where $t_{c,0}$ is the time of initial contact between the particles.

2.2 | Computational fluid dynamics

The fluid phase in CFD-DEM is treated as continuum and is described on the basis of the volume-averaged Navier–Stokes equations, which are discretized on a uniform grid. The equation of continuity and momentum conservation are given by

$$\frac{\partial(\varepsilon_f\rho_f)}{\partial t} + \nabla\cdot(\varepsilon_f\rho_f\mathbf{v}_f) = 0 \tag{6}$$

$$\frac{\partial(\varepsilon_f\rho_f\mathbf{v}_f)}{\partial t} + \nabla\cdot(\varepsilon_f\rho_f\mathbf{v}_f\mathbf{v}_f) = -\varepsilon_f\nabla_p + \nabla\cdot(\varepsilon_f\boldsymbol{\tau}_f) + \mathbf{R}_{f,p} + \varepsilon_f\rho_f\mathbf{g} \tag{7}$$

where ε_f is the fluid volume fraction, ρ_f is the fluid density, $\mathbf{v}_f$ is the fluid velocity, $\boldsymbol{\tau}_f$ is the stress tensor for the fluid phase, $\mathbf{g}$ is gravity, and $\mathbf{R}_{f,p}$ represents the momentum exchange between the fluid and particle phase, expressed as:

$$\mathbf{R}_{f,p} = -\frac{\sum_{p=1}^{N_p}(\mathbf{F}_D^p + \mathbf{F}_L^p)}{V_{cell}} \tag{8}$$

where p is the particle label, N_p is the number of particles in the computational fluid cell, $\mathbf{F}_D^p$ is the drag force acting on particle p due to the fluid, $\mathbf{F}_L^p$ is the lift force acting on particle p due to the fluid, and V_{cell} is the volume of the computational fluid cell. We do not consider two-way coupling of the torque since it has a negligible localized effect on the fluid.

The interaction between the fluid phase and solid particles is resolved through closures for hydrodynamic forces. Correlations used in this work for calculating the drag force, lift force, and hydrodynamic forces are presented below.

Drag force is the strongest force that the fluid exerts on particles and is the main driver of fluidization. In this work we use two approaches to calculate the drag force: the single particle (SP) drag correlation by Hölzer and Sommerfeld,[5] extended with Di Felice's[10] expression to take into account the effect of surrounding particles and by the correlation proposed by Sanjeevi et al.,[16] developed specifically for assemblies of elongated particles.

SP drag force with Di Felice extension. The correlation presented by Hölzer and Sommerfeld[5] can be applied to arbitrary shaped particles where the shape of the particle is taken into account through sphericity, and lengthwise and crosswise sphericity. The drag force coefficient C_D as proposed by Hölzer and Sommerfeld is:

$$C_D = \frac{8}{Re_p}\frac{1}{\sqrt{\Phi_\parallel}} + \frac{16}{Re_p}\frac{1}{\sqrt{\Phi}} + \frac{3}{\sqrt{Re_p}}\frac{1}{\Phi^{3/4}} + 0.42\times10^{0.4(-\log\Phi)^{0.2}}\frac{1}{\Phi_\perp} \tag{9}$$

where Re is the particle Reynolds number $Re = \rho_f d_p\varepsilon_f|\mathbf{v}_f - \mathbf{v}_i|/\eta_f$ with ρ_f the fluid density, d_p the volume-equivalent particle diameter, η_f the fluid viscosity, Φ the particle sphericity, $\Phi_\parallel$ the lengthwise sphericity, and $\Phi_\perp$ the crosswise sphericity.

The effect of surrounding particles (crowding effect) on the drag force experienced by a particle is taken into account through Di Felice's[10] modified drag force expression:

$$\mathbf{F}_D = \frac{1}{2}C_D\rho_f\varepsilon_f^{2-\chi}\frac{\pi}{4}d_p^2|\mathbf{v}_f - \mathbf{v}_i|(\mathbf{v}_f - \mathbf{v}_i) \tag{10}$$

where $\mathbf{v}_f$ is the fluid velocity interpolated to the location of particle i, $\mathbf{v}_i$ is the velocity of particle i, and χ is the Di Felice correction factor given by

$$\chi = 3.7 - 0.65\exp\left[\frac{-(1.5 - \log(\mathrm{Re_p}))^2}{2}\right] \tag{11}$$

where the particle Reynolds number Re is calculated using the expression defined after Equation (9). Note that the appearance of additional factor ϵ_f^2 in Equation (11) comes from the use of a superficial relative velocity in Di Felice's work.

The Di Felice expression was originally developed for spherical particles but because it is one of the few available expressions to take into account crowding effects it has also been applied in simulations of elongated particles fluidization.[1,19,22-25]

Multi-particle drag correlation proposed by Sanjeevi et al.[16] calculates the drag force experienced by a particle as:

$$\mathbf{F}_D = 3\pi\eta_f d_p \bar{F}_{D,\phi}(\mathbf{v}_f - \mathbf{v}_i) \tag{12}$$

where η_f is fluids viscosity, $\bar{F}_{D,\phi}$ is the average drag (normalized by the drag on an isolated volume equivalent sphere) based on particle orientation to the fluid flow. As the average drag $\bar{F}_D$ for different particle incident angles (ϕ) follows a sine-square interpolation, for individual particles[7] as well as assemblies,[16] it can be calculated for any ϕ as:

$$\bar{F}_{D,\phi} = \bar{F}_{D,\phi=0°} + \left(\bar{F}_{D,\phi=90°} - \bar{F}_{D,\phi=0°}\right)\sin^2\phi \tag{13}$$

$\bar{F}_{D,\phi=0°}$ and $\bar{F}_{D,\phi=90°}$ are function of Re and ϕ:

$$\bar{F}_D(\mathrm{Re}, \epsilon_s) = F_{d,isol}\cdot(1-\epsilon_s)^2 + F_{\epsilon_s} + F_{\mathrm{Re},\epsilon_s} \tag{14}$$

The corresponding terms are as follows:

$$F_{d,isol}(Re) = C_{d,isol}\frac{\mathrm{Re}}{24} \tag{15}$$

where $C_{d,isol}$ is calculated as proposed by Sanjeevi et al.[7]:

$$C_{d,isol} = \left(\frac{a_1}{\mathrm{Re}} + \frac{a_2}{\mathrm{Re}^{a_3}}\right)\exp(-a_4\mathrm{Re}) + a_5(1-\exp(a_4\mathrm{Re})) \tag{16}$$

where the coefficients ($a_1...a_5$) for parallel ($\phi = 0°$) and perpendicular ($\phi = 90°$) orientation are given in Table 1.

$$F_{\epsilon_s}(\epsilon_s) = a\sqrt{\epsilon_s}(1-\epsilon_s)^2 + \frac{b\epsilon_s}{(1-\epsilon_s)^2} \tag{17}$$

$$F_{\mathrm{Re},\epsilon_s}(\mathrm{Re}, \epsilon_s) = \mathrm{Re}^c\epsilon_s^d\left(e(1-\epsilon_s) + \frac{f\epsilon_s^3}{(1-\epsilon_s)}\right) + g\epsilon_s(1-\epsilon_s)^2\mathrm{Re} \tag{18}$$

The coefficients for Equations (18) and (19) for parallel and perpendicular orientation are also given in Table 1.

Lift force appears when the long axis of an elongated particle is inclined with respect to the direction of relative fluid flow. The lift

TABLE 1 Coefficients for drag force calculation as proposed by Sanjeevi et al.[7,16]

Coefficient	$\bar{F}_D$			$C_{d,isol}$		
	$\phi = 0°$	$\phi = 90°$			$\phi = 0°$	$\phi = 90°$
a	2	3	a_1		24.48	31.89
b	11.3	17.2	a_2		3.965	5.519
c	0.69	0.79	a_3		0.41	0.229
d	0.77	3	a_4		0.0005	0.0032
e	0.42	11.12	a_5		0.15	1.089
f	4.84	11.12				
g	0	0.57				

force acts in the direction perpendicular to the fluid's relative velocity $\mathbf{v}_{fi}' = \mathbf{v}_f - \mathbf{v}_i$ and lies in the plane defined by the particle long axis orientation vector $\mathbf{u}_i$ and $\mathbf{v}_{fi}'$. The lift force magnitude F_L is multiplied by the lift force orientation vector $\hat{\mathbf{e}}_{L_0}$, which is given as

$$\hat{\mathbf{e}}_{L_0} = \frac{\mathbf{u}_i\cdot\mathbf{v}_{fi}'}{\left|\mathbf{u}_i\cdot\mathbf{v}_{fi}'\right|}\frac{\left(\mathbf{u}_i\times\mathbf{v}_{fi}'\right)\times\mathbf{v}_{fi}'}{\left|\left(\mathbf{u}_i\times\mathbf{v}_{fi}'\right)\times\mathbf{v}_{fi}'\right|} \tag{19}$$

The resultant lift force experienced by a particle is expressed as $\mathbf{F}_L = F_L\hat{\mathbf{e}}_{L_0}$, while the magnitude of lift force is calculated with either the SP correlation proposed by Zastawny et al.[6] or the MP correlation proposed by Sanjeevi et al.[16]

SP lift force. The magnitude of shape induced lift force experienced by an isolated particle is expressed as

$$F_L = \frac{1}{2}C_L\rho_f\frac{\pi}{4}d_p^2|\mathbf{v}_f - \mathbf{v}_i|^2 \tag{20}$$

where C_L is the lift force coefficient calculated using Zastawny et al. correlation[6]:

$$C_{L,\phi} = \left(\frac{b_1}{\mathrm{Re}^{b_2}} + \frac{b_3}{\mathrm{Re}^{b_4}}\right)\sin(\phi)^{b_5+b_6\mathrm{Re}^{b_7}}\cos(\alpha)^{b_8+b_9\mathrm{Re}^{b_{10}}} \tag{21}$$

Fitting coefficients used for the correlation can be found in Table 2.

MP lift force. In this work we have applied a simplified function for shape induced lift force, proposed by Sanjeevi et al.[16] In this simplified approach the average lift force $\bar{F}_L$ (normalized by the drag on an isolated volume equivalent sphere) experienced in a MP system at different ϕ is calculated based on its relation to the normalized drag force as:

$$\bar{F}_{L,\phi} = \left(\bar{F}_{D,\phi=90°} - \bar{F}_{D,\phi=0°}\right)\sin\phi\cos\phi \tag{22}$$

The magnitude of MP lift force is calculated as:

TABLE 2 Coefficients for the lift and torque correlations with the functional form of Zastawny et al.[6] fitted for spherocylinder particles with aspect ratio of 4 using in-house DNS simulations[7]

Lift		Torque	
Coefficient	Value	Coefficient	Value
b_1	1.884	c_1	−2.283
b_2	0.1324	c_2	−0.01145
b_3	0.001668	c_3	4.09
b_4	−0.8159	c_4	−0.01395
b_5	0.8562	c_5	0.3406
b_6	0.003624	c_6	0.3609
b_7	0.6598	c_7	0.1355
b_8	−0.2621	c_8	0.2356
b_9	0.8021	c_9	0.3612
b_{10}	0.04384	c_{10}	0.1358

$$F_L = 3\pi\eta_f d_p \bar{F}_{L,\phi} \,|\mathbf{v}_f - \mathbf{v}_i| \tag{23}$$

Hydrodynamic torque considered in this work is a pitching torque, acting around the axis perpendicular to the plane of relative fluid velocity $\mathbf{v}_{fi}'$ and particle orientation vector $\mathbf{u}_i$. Hence, the torque orientation vector $\hat{\mathbf{e}}_{T_0}$ is given by

$$\hat{\mathbf{e}}_{T_0} = \frac{\mathbf{v}_{fi}' \cdot \mathbf{u}_i}{|\mathbf{v}_{fi}' \cdot \mathbf{u}_i|} \frac{\mathbf{v}_{fi}' \times \mathbf{u}_i}{\left\| \mathbf{v}_{fi}' \times \mathbf{u}_i \right\|} \tag{24}$$

The resultant torque is then expressed as $\mathbf{T}_P = T_P \hat{\mathbf{e}}_{T_0}$.

SP hydrodynamic torque. The magnitude of the hydrodynamic torque on an isolated particle is calculated as proposed by Zastawny et al.[6]

$$T_P = \frac{1}{2} C_T \rho_f \frac{\pi}{8} d_p^3 |\mathbf{v}_f - \mathbf{v}_i|^2 \tag{25}$$

where C_T is the torque coefficient calculated using Zastawny et al. correlation:

$$C_{T,\alpha} = \left(\frac{c_1}{Re^{c_2}} + \frac{c_3}{Re^{c_4}} \right) \sin(\phi)^{c_5 + c_6 Re^{c_7}} \cos(\phi)^{c_8^Z + c_9^Z Re^{c_{10}^Z}} \tag{26}$$

MP *hydrodynamic torque.* The magnitude of MP hydrodynamic torque proposed by Sanjeevi et al.[16] is calculated as:

$$T_P = 2\pi\eta_f d_p^2 \bar{T}_{P,\phi} \,|\mathbf{v}_f - \mathbf{v}_i| \tag{27}$$

where $\bar{T}_{P,\phi}$ is average hydrodynamic torque for MP system, calculated by Sanjeevi et al. correlation:

$$\bar{T}_{P,\phi}(Re, \epsilon_s, \phi) = T_{P,mag}(Re, \epsilon_s) \sin\phi \cos\phi \tag{28}$$

with

$$T_{P,mag}(Re, \epsilon_s) = T_{p,isol}(Re) \cdot (1 - \epsilon_s)^2 + T_{Re,\epsilon_s}(Re, \epsilon_s) \tag{29}$$

TABLE 3 Coefficients for torque calculation (Equation 31) as proposed by Sanjeevi et al.[16]

Coefficients	T_{Re,ϵ_s}
a	0.82
b	1.44
c	1.07
d	5.48
e	0.223

$$T_{Re,\epsilon_s}(Re, \epsilon_s) = Re^a \epsilon_s{}^b \left(c(1 - \epsilon_s) + \frac{d\epsilon_s{}^3}{(1 - \epsilon_s)} \right) + e\epsilon_s(1 - \epsilon_s)^2 Re \tag{30}$$

Coefficients for Equation (31) are given in Table 3.

3 | SIMULATION PARAMETERS

Simulations were done for a rectangular fluidized bed, whose dimensions are the same as in previous MPT experiments[17] and numerical investigation.[1] The column dimensions and main parameters necessary for the CFD-DEM simulation are presented in Table 4. The particles used in this investigation are capsule-like spherocylinders with aspect ratio of 4. The DEM parameters for particles were determined experimentally by Mahajan et al.[26] for particles made of alumide, a 3D printing material consisting of a mixture of aluminum and nylon. The minimum fluidization velocities were determined experimentally[17] and particle properties are listed in Table 5.

The standard practice for choosing the grids size in CFD-DEM simulations for spherical particles is that the grid dimensions should be between $1.6d_p$ and $5d_p$.[27,28] For the particle and column dimensions used in this work a grid size of $2.83d_p$ was applied, where d_p is the diameter of a volume equivalent sphere. This grid size satisfies both standard practice for spherical particles and offers a cell size larger than the length of the spherocylindrical particle.[1]

4 | RESULTS

We will investigate the distributions of particle orientation and particle velocity along the vertical (z-)axis for two different inlet gas velocities ($1.6U_{mf}$ and $2U_{mf}$). Two simulation cases will be compared, the first with SP correlations and the second with MP correlations. For the SP case, the general Hölzer–Sommerfeld drag equation, with a simple correction for the MP effect, is used. This is the most common approach found in literature to deal with hydrodynamic forces on nonspherical particles in dense systems. Table 6 lists correlations applied in each case. The simulation results are compared with experimental results obtained in our previous work using MPT technique.[17] More technical information about the MPT experimental technique can be found in the work by Buist et al.[29]

4.1 | Particle orientation

In this section, we analyze the average particle orientation in the terms of the z-component of the particle orientation vector **u**. Figure 2 shows the time averaged distribution of the particle orientation relative to the z-axis (direction of the fluid flow). If $|u_z| = 0$, the particle has a horizontal orientation and is perpendicular to the fluid flow, while for $|u_z| = 1$, the particle is oriented vertically and is fully aligned with the fluid flow. Note that for fully randomly oriented particles, the expected distribution of $|u_z|$ is flat.

From Figure 2, it can be seen that MP correlations show slightly better agreement with experimental results compared to SP correlations. This is specifically the case for predicting the fraction of particles oriented vertically ($|u_z|$ close to 1). However in some regions, specifically for $|u_z|$ around 0, SP correlations show better agreement with the experimental results. The difference between MP and SP correlations is considerably larger for $|u_z|$ near 1 then near 0 and it can be observed that the difference between MP correlations and MPT experiments for horizontally oriented particles is less notable than the over-prediction of the fraction of particles oriented vertically in case of SP correlations compared to MPT experiments.

Figure 2b shows that an increase in fluid velocity leads to an increase of the fraction of vertically aligned particles and a reduction of horizontally aligned particles. The difference between MP and SP correlations is also considerably smaller for $2U_{mf}$ compared to $1.6U_{mf}$, but the same conclusions still apply.

Figures 3 and 4 give more insight into the preferred particle orientation in different parts of the fluidized bed. The preferred particle orientation is determined based on the particle orientation tensor **S**, calculated using the expression

$$\mathbf{S} = \begin{bmatrix} \langle u_x^2 \rangle & \langle u_x u_y \rangle & \langle u_x u_z \rangle \\ \langle u_y u_x \rangle & \langle u_y^2 \rangle & \langle u_y u_z \rangle \\ \langle u_z u_x \rangle & \langle u_z u_y \rangle & \langle u_z^2 \rangle \end{bmatrix}. \tag{31}$$

The diagonal components of this tensor can be used to determine the preferred alignment in the reactor. If the difference between the diagonal components is less than 0.1 that is, $\left|\langle u_x^2 \rangle - \langle u_y^2 \rangle\right| < 0.1$, $\left|\langle u_x^2 \rangle - \langle u_z^2 \rangle\right| < 0.1$, and $\left|\langle u_y^2 \rangle - \langle u_z^2 \rangle\right| < 0.1$, the particle is considered to be randomly oriented. On the other hand, if one component is considerably larger than the other two components, we conclude that the particle is preferentially aligned with the corresponding axis. Figures 3 and 4 show time averaged preferred particle orientation in the x–z plane for a cross section cutting through the center of the bed in the y-direction (6 cm ≤ y ≤ 7.5 cm).

From Figures 3 and 4, the improved prediction of particle orientation by MP correlations becomes more evident. Looking at the lower part of the column (z-position ≤30 cm) it is clear that MP correlations show better agreement with experimental results and that SP correlations over-predict the amount of regions in which particles are preferably oriented vertically. With an increase of the fluid velocity (Figure 4) there is an increase in the amount of regions where particles preferably align vertically, in the lower part of the bed (z-position ≤30 cm) and in the wall region. From Figure 4, it can still be inferred that MP correlations have better agreement with experimental results in the lower part of the bed and in the wall region. In the case of SP correlations (Figure 4a), in the lower part of the bed the over-prediction of particles oriented vertically is noticeable, but also in the higher parts, near walls the SP results differ from the experimental results more than in case of MP correlations.

In the higher parts of the bed (z-position >30 cm), Figures 3 and 4, show that the simulations results predict a higher preference for

TABLE 4 Relevant parameters for the CFD-DEM algorithm

CFD parameters		
Parameter	**Symbol**	**Value**
Reactor base	L_x, L_y	0.15 m, 0.15 m
Reactor height	H_z	1.05 m
Number of grid cells	n_x^g, n_y^g, n_z^g	$10 \times 10 \times 70$
Grid cell dimensions	$c_x = c_y = c_z$	0.015 m
Time step	t_{CFD}	1×10^{-4} s
Fluid density	ρ_f	1.2 kg/m^3
Fluid viscosity	η_f	$1.568 \cdot 10^{-5}$ Pa s
DEM parameters		
Parameter	**Symbol**	**Value**
Time step	t_{DEM}	1×10^{-5} s
Coefficient of friction	μ	0.46
Coefficient of rolling friction	μ_r	0.46
Coefficient of restitution	e	0.43

TABLE 5 Particle properties

Particles	
Parameter	**Value**
Number of particles	32,500
Particle length [L]	12 mm
Particle diameter [2R]	3 mm
Particle density	1,442 kg/m^3
Minimum fluidization velocity [U_{mf}]	1.7 m/s

TABLE 6 Correlations applied for single particle (SP) correlations and multiparticle (MP) correlations

Case	Drag force	Lift force	Torque
SP-correlations	Hölzer-Sommerfeld[5] + Di Felice[10]	Zastawny et al.[6]	Zastawny et al.[6]
MP-correlations	Sanjeevi et al.[16]	Sanjeevi et al.[16]	Sanjeevi et al.[16]

(a)

(b)
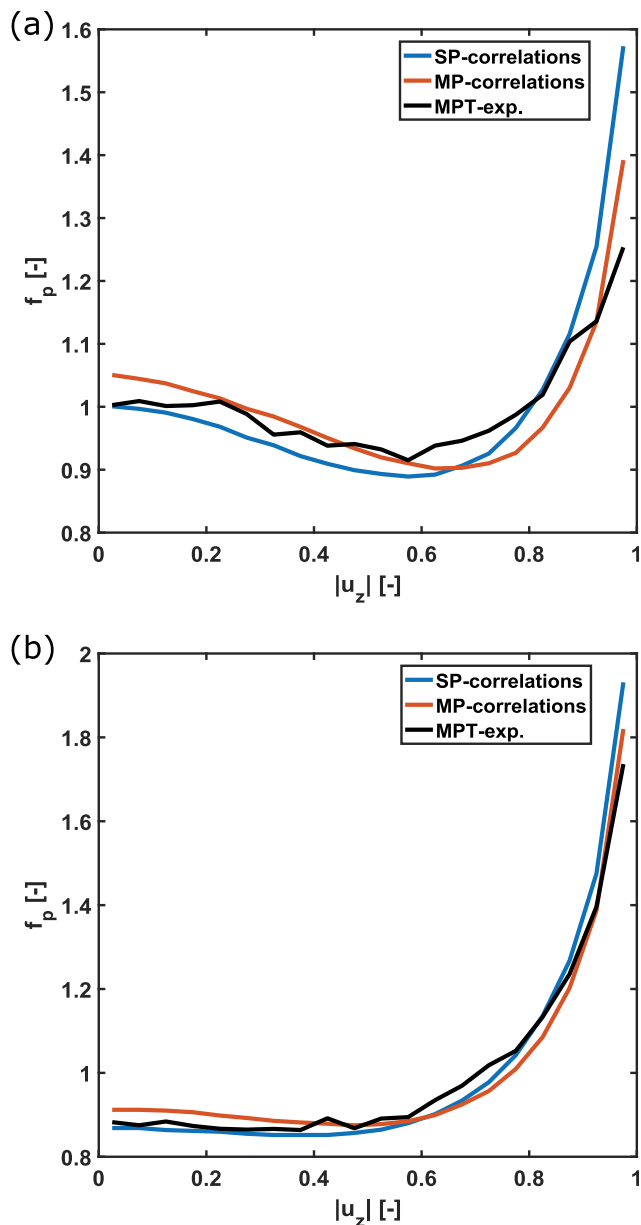
FIGURE 2 Probability distribution function for the particle orientation at (a) $1.6U_{mf}$ and (b) $2U_{mf}$. Simulations with single (SP) and multi (MP) particle correlations are compared with MPT experiments [Color figure can be viewed at wileyonlinelibrary.com]

FIGURE 3 Preferred orientation of particles in the grid cells of the reactor for (a) single-particle, (b) multi-particle correlations, and (c) experimental results at $1.6U_{mf}$. Here the color scheme is: blue squares (■) are x-aligned, green squares (■) are y-aligned, red squares (■) are z-aligned, and cyan squares (■) are randomly orientated. White space represents empty cells [Color figure can be viewed at wileyonlinelibrary.com]

the particles to orient horizontally, compared to the experimental results where particles are more randomly oriented. This is more evident in the case of MP correlations, particularly at the gas velocity of $2U_{mf}$ (Figure 4b). In this region, the SP correlations show better agreement with experimental results.

However, as can be seen in Figure 5, above 30 cm in the z-direction the average cell occupancy is dropping dramatically and above 40 cm there is on average less than 1 particle per cell. The region above the height of 30 cm can therefore be considered as the free-board region, where the crowding effect is considerably lower compared to the dense fluidized region below 30 cm. It should also be

noted that in the free-board region, the average occupancy predicted by the simulations in all cases starts to differ from the experimental results.

## 4.2 | Effect of lift force and hydrodynamic torque on particle orientation

In our previous work, we have investigated the effects of SP shape induced lift force and hydrodynamic torque on the particle orientation.[1] We have shown that hydrodynamic torque has a major effect on the particle orientation and leads to a change of preferred particle orientation from vertical to more horizontal. Here we extend the analysis to MP correlations and make a detailed comparison with experimental results. In detail, we will compare the simulation results of cases using the Sanjeevi et al.[16] MP correlations considering: 1. drag force only (D), 2. drag force and shape induced lift force (D + L), 3. drag force and hydrodynamic torque (D + T), and 4. drag force with lift force and hydrodynamic torque (D + L + T), to the experimental MPT results. Figure 6 shows the time-average fraction of particles with a certain orientation to the z-axis.

It is clear that cases where hydrodynamic torque is not considered show a strong preference for particles to align with the fluid flow and that they are not at all representing what is observed in
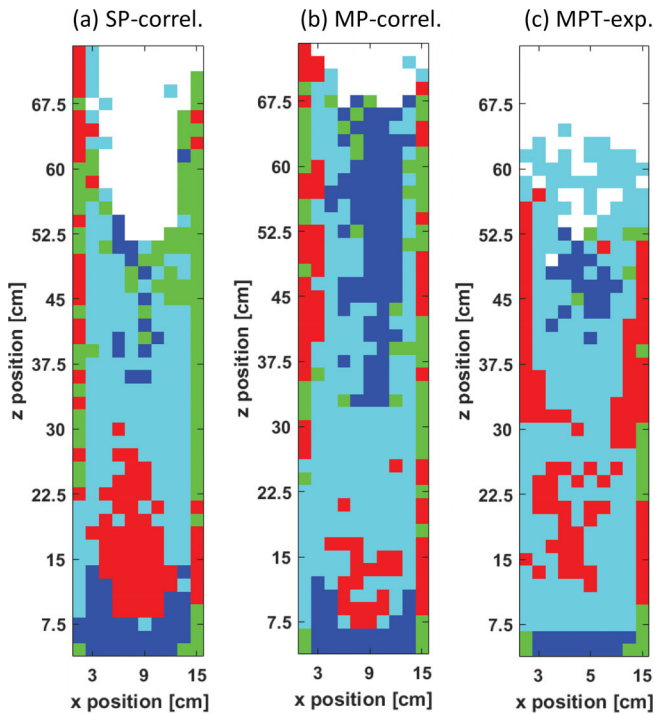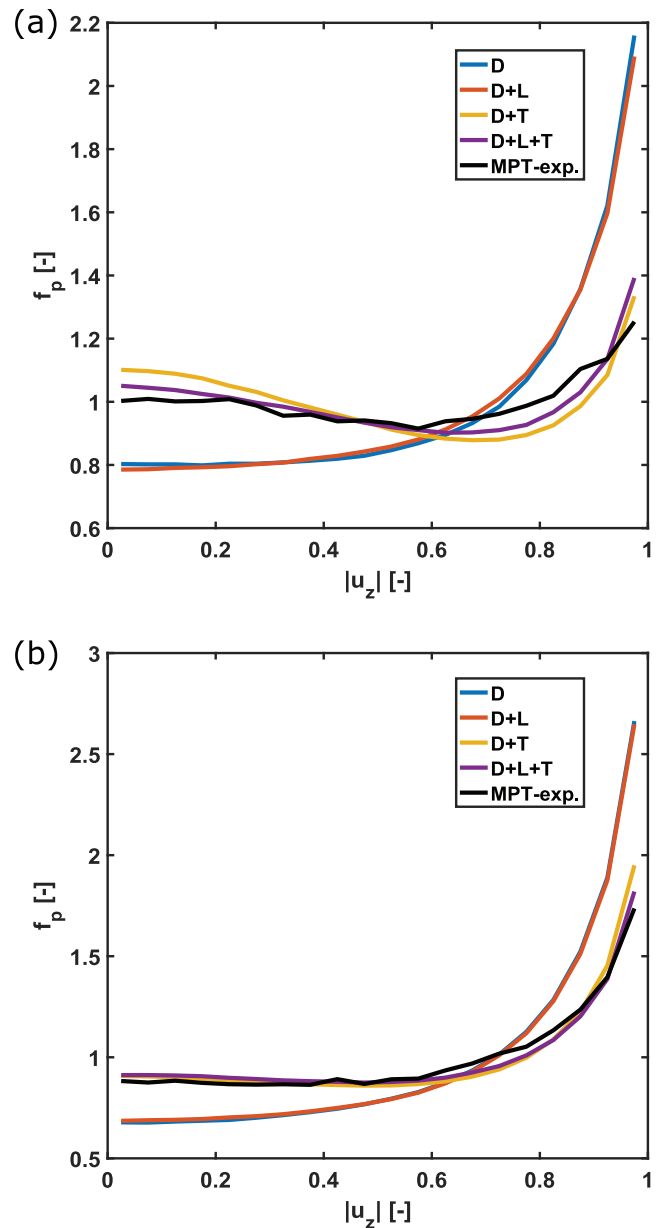
FIGURE 4 Preferred orientation of particles in the grid cells of the reactor for (a) single-particle, (b) multi-particle correlations, and (c) experimental results at $2U_{mf}$. Here the color scheme is: blue squares (■) are x-aligned, green squares (■) are y-aligned, red squares (■) are z-aligned, and cyan squares (■) are randomly orientated. White space represents empty cells [Color figure can be viewed at wileyonlinelibrary.com]
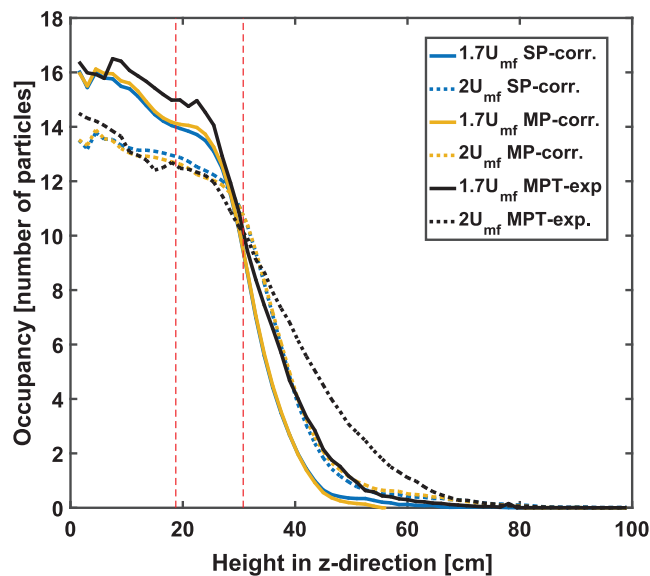
FIGURE 5 Average cell occupancy along the height in z-direction. The dashed red lines indicate the positions along the z-axis used for the sampling of v_z profiles in Section 4.3 [Color figure can be viewed at wileyonlinelibrary.com]

FIGURE 6 Preferred particle orientation at (a) $1.6U_{mf}$ and (b) $2U_{mf}$. Variation of $f_p(|u_z|)$ for simulations with differing hydrodynamic force conditions and from experimental results [Color figure can be viewed at wileyonlinelibrary.com]

are oriented horizontally, perpendicular to the direction of the fluid flow. The simulations in which hydrodynamic torque is considered are almost perfectly matching the results obtained from the experiments. Note that including lift in addition to torque increases the agreement some more, but the effect is relatively small. Finally, as mentioned before, an increase of gas velocity leads to an increase of the fraction of particles oriented vertically while reducing the fraction of particle oriented horizontally.

Figures 7 and 8 show the time averaged preferred particle orientation in the z–x plane for a cross section in cutting through the center of the bed (as explained in Section 4.1) for cases with different MP hydrodynamic forces considered and the ones obtained

experimental results. Including hydrodynamic torque reduces the fraction of particles oriented vertically and leads to randomization of particle orientations but also to a considerable increase of particles that

experimentally. It can be seen that including hydrodynamic torque leads to randomization of the particle orientation in the middle section of the bed, but also to a considerable increase of horizontally oriented particles in the free-board region. Even though hydrodynamic torque has the biggest effect on particle orientation, Figures 3 and 4 show that actually cases where both lift force and hydrodynamic torque are considered have the best agreement with experimental results.

4.3 | Particle velocity along z-axis

The particle velocity along the vertical direction (z-axis) is sampled at two bed heights, as indicated in Figure 5. The lower position in the bed (z = 18.75 cm) corresponds to dense fluidizing conditions, while the higher position (z = 30.75 cm) corresponds to the free-board region where the particle flow is getting more diluted and the agreement between simulation and experimental

FIGURE 7 Preferred orientation of particles in the grid cells of the reactor for case with multi-particle (a) drag force only, (b) drag and lift force, (c) drag and hydrodynamic torque, and (d) 2MPT experiments, at 1.6U_mf. Here the color scheme is: blue squares (■) are x-aligned, green squares (■) are y-aligned, red squares (■) are z-aligned, and cyan squares (■) are randomly orientated. White space represents empty cells [Color figure can be viewed at wileyonlinelibrary.com]
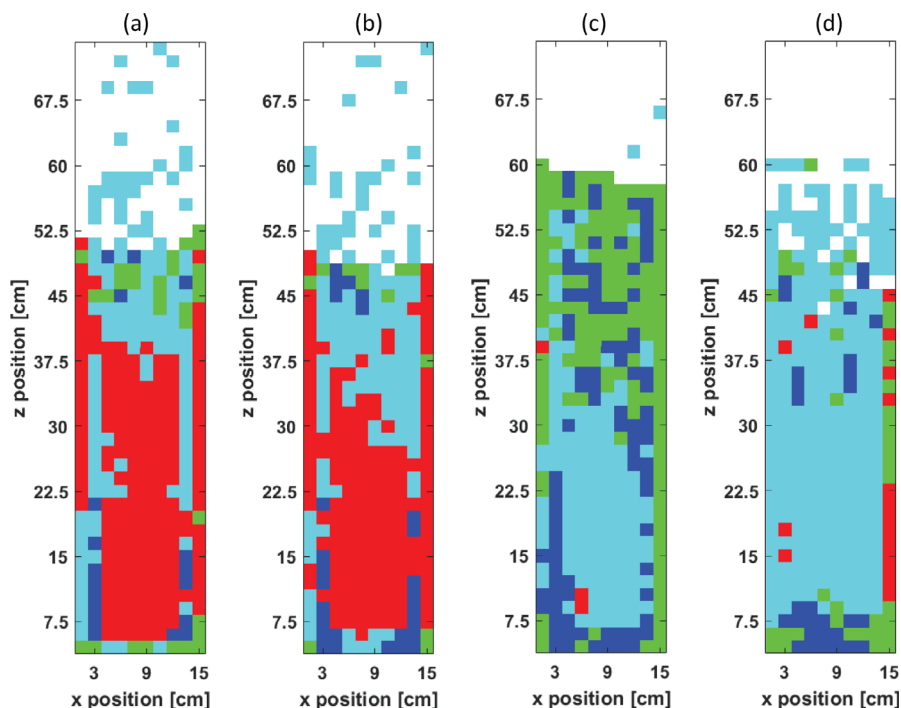
FIGURE 8 Preferred orientation of particles in the grid cells of the reactor for case with multi-particle (a) drag force only, (b) drag and lift force, (c) drag and hydrodynamic torque, and (d) MPT experiments, at 2U_mf. Here the color scheme is: blue squares (■) are x-aligned, green squares (■) are y-aligned, red squares (■) are z-aligned, and cyan squares (■) are randomly orientated. White space represents empty cells [Color figure can be viewed at wileyonlinelibrary.com]
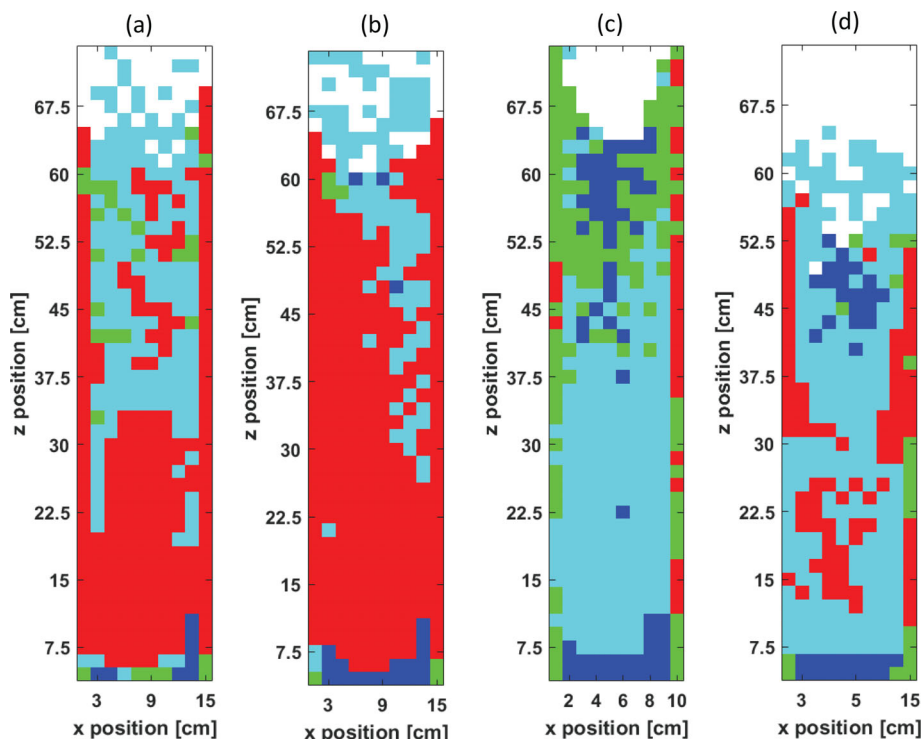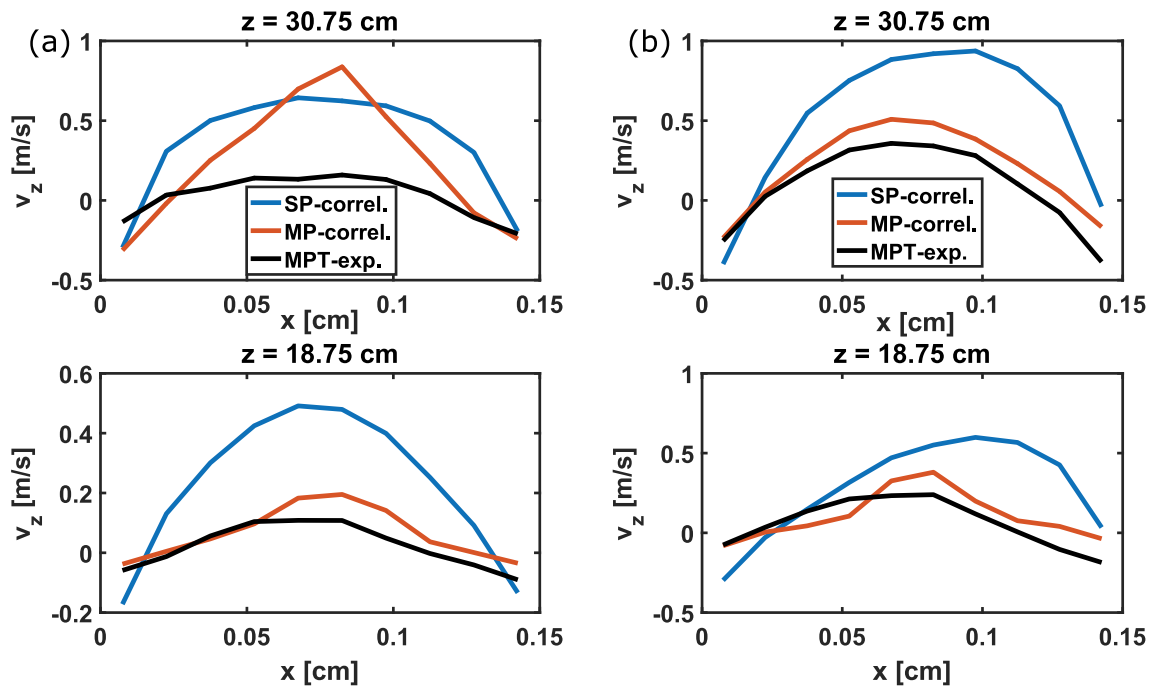
FIGURE 9 Comparison of the temporally-averaged vertical solids velocity v_z along the x-axis at two bed heights and at (a) $1.6U_{mf}$ and (b) $2U_{mf}$ [Color figure can be viewed at wileyonlinelibrary.com]

results in terms of average occupancy is still good. The time averaged z-velocities are presented along x-axis in the plane cutting through the center of the bed (6 cm $\leq y \leq$ 7.5 cm). Particle velocities are weighted by the number of particles in the cell at each time step, that is, they are a measure for the average solids flux.

Figure 9 shows the time averaged particle z-velocities at two positions in the bed and at two inlet gas velocities. A considerable difference between SP and MP correlations can be seen in all cases. It is clear that SP correlations over-predict the particle z-velocities and that MP correlations show much better agreement with the experimental results. At the higher position in the bed (z = 30.75 cm) and for the lower gas velocity of $1.6U_{mf}$, over-prediction of the vertical solids velocity can be seen for both SP and MP correlations. This can be caused by the more diluted particle flow at this position. As discussed in Section 4.1, in the free-board region MP correlations can give less accurate predictions. With an increase of gas velocity to $2U_{mf}$, the particle flow gets denser at the higher position in the bed and again MP correlations show much better agreement with experimental results than SP correlations.

5 | CONCLUSION

In this work, we applied CFD-DEM simulations to look into the effect and importance of MP correlations for hydrodynamic forces and torque. Simulation results were compared to the results obtained using MPT experiments. MP correlations considerably

improved prediction of average particle orientation and its distribution throughout the fluidized bed, in dense fluidizing conditions. Usage of SP correlations leads to over-prediction of the number of particles that align vertically in the lower part of the fludized bed. On the other hand, MP correlations over-predict the number of particles that orient horizontally in the free-board region. Comparing to experimental results, this over-prediction in the free-board region is encountered in simulations with SP correlations too, however to a smaller extent. Simulations with MP correlations also show better agreement with experimental results in dense fluidizing conditions concerning the particle velocity in the vertical direction. Using SP correlations leads to considerable over-prediction of the particle velocities in all cases.

Even though SP correlations show better agreement with experimental results in the free-board region, during the fluidization process particles spend most of their time in dense fluidizing conditions and only small number of individual particles gets lifted in to the free-board region. This is why it is more important to get proper behavior of particles in the dense fluidizing conditions. We therefore expect that usage of MP correlations will lead to considerable improvement in simulation of elongated particle fluidization.

ORCID

Ivan Mema https://orcid.org/0000-0003-2587-8613

REFERENCES

1. Mema I, Mahajan VV, Fitzgerald BW, Padding JT. Effect of lift force and hydrodynamic torque on fluidisation of non-spherical particles. *Chem Eng Sci*. 2019;195:642-656. https://doi.org/10.1016/j.ces.2018.10.009.

2. Goossens WR. Review of the empirical correlations for the drag coefficient of rigid spheres. *Powder Technol*. 2019;352:350-359. https://doi.org/10.1016/j.powtec.2019.04.075.

3. Haider A, Levenspiel O. Drag coefficient and terminal velocity of spherical and nonspherical particles. *Powder Technol*. 1989;58(1):63-70. https://doi.org/10.1016/0032-5910(89)80008-7.

4. Ganser GH. A rational approach to drag prediction of spherical and nonspherical particles. *Powder Technol*. 1993;77(2):143-152. https://doi.org/10.1016/0032-5910(93)80051-b.

5. Hölzer A, Sommerfeld M. New simple correlation formula for the drag coefficient of non-spherical particles. *Powder Technol*. 2008;184(3):361-365. https://doi.org/10.1016/j.powtec.2007.08.021.

6. Zastawny M, Mallouppas G, Zhao F, van Wachem B. Derivation of drag and lift force and torque coefficients for non-spherical particles in flows. *Int J Multiphase Flow*. 2012;39:227-239.

7. Sanjeevi SK, Kuipers J, Padding JT. Drag, lift and torque correlations for non-spherical particles from stokes limit to high Reynolds numbers. *Int J Multiphase Flow*. 2018;106:325-337. https://doi.org/10.1016/j.ijmultiphaseflow.2018.05.011.

8. Cao Z, Tafti D, Shahnam M. Development of drag correlation for suspensions of ellipsoidal particles. *Powder Technol*. 2020;369:298-310. https://doi.org/10.1016/j.powtec.2020.05.049.

9. Ouchene R, Khalij M, Arcen B, Tanière A. A new set of correlations of drag, lift and torque coefficients for non-spherical particles and large Reynolds numbers. *Powder Technol*. 2016;303:33-43. https://doi.org/10.1016/j.powtec.2016.07.067.

10. Felice RD. The voidage function for fluid-particle interaction systems. *Int J Multiphase Flow*. 1994;20(1):153-159.

11. Tenneti S, Garg R, Subramaniam S. Drag law for monodisperse gas–solid systems using particle-resolved direct numerical simulation of flow past fixed assemblies of spheres. *Int J Multiphase Flow*. 2011;37(9):1072-1092. https://doi.org/10.1016/j.ijmultiphaseflow.2011.05.010.

12. Tang YY, Peters EAJFF, Kuipers JAMH, Kriebitzsch SHLS, van der Hoef MAM. A new drag correlation from fully resolved simulations of flow past monodisperse static arrays of spheres. *AIChE J*. 2014;61(2):688-698. https://doi.org/10.1002/aic.14645.

13. Rong L, Dong K, Yu A. Lattice-boltzmann simulation of fluid flow through packed beds of uniform spheres: effect of porosity. *Chem Eng Sci*. 2013;99:44-58. https://doi.org/10.1016/j.ces.2013.05.036.

14. Li X, Jiang M, Huang Z, Zhou Q. Effect of particle orientation on the drag force in random arrays of prolate ellipsoids in low-Reynolds-number flows. *AIChE J*. 2019;65(8). https://doi.org/10.1002/aic.16621.

15. He L, Tafti D. Variation of drag, lift and torque in a suspension of ellipsoidal particles. *Powder Technol*. 2018;335:409-426. https://doi.org/10.1016/j.powtec.2018.05.031.

16. Sanjeevi SKP, Padding JT. Hydrodynamic forces on monodisperse assemblies of axisymmetric elongated particles: orientation and voidage effects. *AIChE J*. 2020;66(6). https://doi.org/10.1002/aic.16951.

17. Mema I, Buist KA, Kuipers JAM, Padding JT. Fluidization of spherical versus elongated particles: experimental investigation using magnetic particle tracking. *AIChE J*. 2019;66(4). https://doi.org/10.1002/aic.16895.

18. Kloss C, Goniva C, Hager A, Amberger S, Pirker S. Models, algorithms and validation for opensource DEM and CFD-DEM. *Prog Comp Fluid Dynamics*. 2012;12(2/3):140. https://doi.org/10.1504/pcfd.2012.047457.

19. Mahajan VV, Nijssen TM, Kuipers J, Padding JT. Non-spherical particles in a pseudo-2d fluidised bed: modelling study. *Chem Eng Sci*. 2018;192:1105-1123. https://doi.org/10.1016/j.ces.2018.08.041.

20. Cundall PA, Strack ODL. A discrete numerical model for granular assemblies. *Géotechnique*. 1979;29(1):47-65. https://doi.org/10.1680/geot.1979.29.1.47.

21. Vega C, Lago S. A fast algorithm to evaluate the shortest distance between rods. *Comput Chem*. 1994;18(1):55-59. https://doi.org/10.1016/0097-8485(94)80023-5.

22. Oschmann T, Hold J, Kruggel-Emden H. Numerical investigation of mixing and orientation of non-spherical particles in a model type fluidized bed. *Powder Technol*. 2014;258:304-323. https://doi.org/10.1016/j.powtec.2014.03.046.

23. Vollmari K, Jasevičius R, Kruggel-Emden H. Experimental and numerical study of fluidization and pressure drop of spherical and non-spherical particles in a model scale fluidized bed. *Powder Technol*. 2016;291:506-521. https://doi.org/10.1016/j.powtec.2015.11.045.

24. Ma H, Zhao Y. CFD-DEM investigation of the fluidization of binary mixtures containing rod-like particles and spherical particles in a fluidized bed. *Powder Technol*. 2018;336:533-545. https://doi.org/10.1016/j.powtec.2018.06.034.

25. Shrestha S, Kuang S, Yu A, Zhou Z. Orientation of spheroidal particles in single jet bubbling fluidized beds. *Powder Technol*. 2020;361:363-373. https://doi.org/10.1016/j.powtec.2019.07.095.

26. Mahajan VV, Padding JT, Nijssen TMJ, Buist KA, Kuipers JAM. Non-spherical particles in a pseudo-2d fluidised bed: experimental study. *AIChE J*. 2018;64(5):1573-1590. https://doi.org/10.1002/aic.16078.

27. Deen N, Annaland MVS, der Hoef MV, Kuipers J. Review of discrete particle modeling of fluidized beds. *Chem Eng Sci*. 2007;62(1–2):28-44. https://doi.org/10.1016/j.ces.2006.08.014.

28. Peng Z, Doroodchi E, Luo C, Moghtaderi B. Influence of void fraction calculation on fidelity of CFD-DEM simulation of gas-solid bubbling fluidized beds. *AIChE J*. 2014;60(6):2000-2018. https://doi.org/10.1002/aic.14421.

29. Buist KA, van der Gaag AC, Deen NG, Kuipers JAM. Improved magnetic particle tracking technique in dense gas fluidized beds. *AIChE J*. 2014;60(9):3133-3142. https://doi.org/10.1002/aic.14512.